Geophysical Research Letters

RESEARCH LETTER
10.1029/2021GL097018

Key Points:

- The seismic P- and S-wave structures from wide-angle seismic data yield a Poisson's ratio model beneath the Nazca Ridge (NR) prior to subduction
- The NR presents a lower crust with Poisson's ratios of 0.28 ± 0.02 consistent with a high concentration of Mg
- The thick NR crust (~15 km) is consistent with an elevation of the asthenospheric mantle potential temperature in ~100°C

Supporting Information:

Supporting Information may be found in the online version of this article.

Correspondence to:

E. Contreras-Reyes,
edcontrr@uchile.cl

Citation:

Contreras-Reyes, E., Obando-Orrego, S., Cortés-Rivas, V., & Krabbenhoeft, A. (2022). Poisson's ratio structure beneath the Nazca Ridge. *Geophysical Research Letters*, *49*, e2021GL097018. https://doi.org/10.1029/2021GL097018

Received 15 NOV 2021
Accepted 22 APR 2022

Author Contributions:

Conceptualization: E. Contreras-Reyes, V. Cortés-Rivas, A. Krabbenhoeft
Data curation: E. Contreras-Reyes, S. Obando-Orrego, V. Cortés-Rivas
Formal analysis: E. Contreras-Reyes, A. Krabbenhoeft
Investigation: E. Contreras-Reyes, A. Krabbenhoeft
Methodology: E. Contreras-Reyes, S. Obando-Orrego, V. Cortés-Rivas
Project Administration: A. Krabbenhoeft
Resources: A. Krabbenhoeft
Software: S. Obando-Orrego, V. Cortés-Rivas
Supervision: E. Contreras-Reyes
Validation: E. Contreras-Reyes, V. Cortés-Rivas
Writing – original draft: E. Contreras-Reyes, V. Cortés-Rivas, A. Krabbenhoeft

Poisson's Ratio Structure Beneath the Nazca Ridge

E. Contreras-Reyes[1], S. Obando-Orrego[1], V. Cortés-Rivas[2], and A. Krabbenhoeft[3]

[1]Departamento de Geofísica, Facultad de Ciencias Físicas y Matemáticas, Universidad de Chile, Santiago, Chile, [2]Northern Arizona University, Flagstaff, AZ, USA, [3]GEOMAR-Helmholtz Centre for Ocean Research, Kiel, Germany

Abstract The Nazca Ridge (NR) was formed near the interaction of a hotspot mantle plume and an active spreading center. We use active-source wide-angle seismic data to obtain 2-D V_p and V_s tomographic models, and hence the Poisson's ratio (ν) structure beneath the NR. Results show a ~2 km thick seismic layer 2A with ν values of 0.25–0.32 in the uppermost crust interpreted as pillow basalts with a low degree of fracturing and/or hydrothermal alteration. The 2A/B boundary layer presents ν values of 0.27–0.29 consistent with pillow basalts/sheeted dykes units. A ~3 km layer 2B overlies a ~10 km layer 3 with ν values of 0.24–0.3 at the 2/3 boundary layer. The lowermost layer 3 presents ν values of 0.28 ± 0.02 suggesting an increase in Mg content (≥10% wt). The NR crust (~15 km thick) requires an increment of the asthenospheric mantle potential temperature in ~100°C formed by passive adiabatic decompression melting.

Plain Language Summary The interaction of a hot mantle plume with an overlying moving oceanic plate results in hotspot volcanic activity, and the formation of large volcanoes (hotspot tracks). This process is enhanced in a setting where the hotspot mantle plume is located near an active spreading center or mid ocean ridge such as the East Pacific Rise or Middle Atlantic Ridge. The Nazca Ridge (NR) is a hotspot track located off South America at present and was formed 30–45 Ma by the interaction of the Easter Island hotspot mantle plume with the Farallon-Nazca plate near the East Pacific Rise. Our geophysical results show that the NR presents an anomalously thick oceanic crust (~15 km thick), which is about 2.5 times thicker than normal crust of the Pacific Ocean. The rocks at the base of the crust presents likely an increase in magnesium content. This is consistent with the intrusion of voluminous magmatic material during the interaction of the hotspot plume with the oceanic plate at anomalously high temperatures compared with the surrounding mantle.

1. Introduction

Seismic studies reveal the deep structure of hotspot tracks formed by the interaction of a hotspot mantle plume and the overlying oceanic lithosphere (e.g., Richards et al., 2013). Results include the seismic structure beneath Hawaii (Watts et al., 2021), the Marquesas Hotspot province (Caress et al., 1995), Louisville Ridge (Contreras-Reyes et al., 2010), La Reunion (Charvis et al., 1999); the Marcus-Wake seamount chain (Kaneda et al., 2010), Juan Fernández Ridge (Kopp et al., 2004), Great Meteor Seamount (Weigel & Grevemeyer, 1999), Shatzky Ridge (Korenaga & Sager, 2012), Cocos and Carnegie Ridges (Galapagos hotspot track; Sallarès et al., 2003; Walther, 2003) among others (see Richards et al. (2013) for a compilation). Some results show relatively low uppermost mantle P-wave velocity (V_p) values higher than lower crustal/gabbroic rocks (7.0–7.2 km/s) but lower than typical peridotite/dunite mantle rocks (8.0–8.3 km/s) beneath hotspot provinces formed on mature oceanic lithosphere (>30 Ma; Hawaii, La Reunion, and Marquesas cases). These relatively low "uppermost mantle" V_p zones have been interpreted as hotspot magmatic material intruded as a deep-crustal underplating (Caress et al., 1995; Charvis et al., 1999; Richards et al., 2013; Watts et al., 2021).

Seismic results also show anomalously thick lower crust (10–15 km thick) with lowermost crustal V_p values of 6.9–7.2 km/s for the case of oceanic ridges formed by a hotspot mantle plume positioned near a spreading center. Examples include the Cocos, Malpelo, and Carnegie Ridges (Sallarès et al., 2003, 2005). Furthermore, Walther (2003) reported lowermost crustal V_p values of 7.2–7.3 km/s for the Cocos Ridge interpreted as normal gabbroic rocks under increased pressure at depths of 15 km bsf.

The Nazca Ridge (NR) was formed near the interaction of a hotspot mantle plume (Easter Island/Sala y Gómez hotspot system) and an active spreading center (East Pacific Rise; Naar & Hey, 1986; Bello-González et al., 2018). Geophysical studies have been carried out during the last two decades in the easternmost portion of the NR near the Peruvian trench (Figure 1; Contreras-Reyes et al., 2019, 2021; Hampel et al., 2004; Krabbenhoeft et al., 2004).

Writing – review & editing: E. Contreras-Reyes

V_p models show that the NR is formed of anomalously oceanic crust ~15 km thick and exhibits lowermost crustal velocities of 7.2–7.5 km/s (Contreras-Reyes et al., 2019; Hampel et al., 2004). North of the NR-trench collision zone (9°, 12°, and 14°S), seismic (Krabbenhoeft et al., 2004) and gravimetric (Contreras-Reyes et al., 2021) models show that the Nazca oceanic crust is ~6 km thick and presents typical lowermost crustal velocities and densities of 7.0–7.2 km/s and 2,850 kg/m^3, respectively. Moreover, results from flexural, gravimetric, active-, and natural-seismic models for the NR near the Peruvian trench suggest that bend faulting and hydration is confined only to shallow levels (upper or lower crust; Contreras-Reyes et al., 2019, 2021; Kumar et al., 2016; Wagner et al., 2020).

Nonetheless, our knowledge of the deep seismic structure of hotspot tracks came mainly from wide-angle seismic studies that provide estimates only on the P-wave velocity structure. By contrast, S-wave velocity (V_s) studies of relatively high resolution obtained from wide-angle seismic data are scarce due to the difficulty in recording S-wave arrivals of relative high amplitude. Some exceptions have focused on the V_s modeling of the oceanic crust in trench-outer rise settings (Contreras-Reyes et al., 2008; Fujie et al., 2013; Moscoso & Grevemeyer, 2015) or in rifting to seafloor spreading regions (Lata & Dunn, 2020; Shuck et al., 2019), however, the V_s structure beneath hotspot tracks is poorly constrained (Trummer, 2002). Estimates of both V_p and V_s provide better constraints for lithological composition, hydration, and metamorphism degree than V_p alone (Christensen, 1996; Hyndman, 1979).

In this study, we model converted S-wave arrivals recorded along a single seismic line oriented perpendicular to the NR axis near the Peruvian trench (~15°S; Figure 1). We present V_p and V_s tomographic 2-D models beneath the NR to investigate magmatic processes during the interaction between a hot mantle plume system and an active spreading center. The presented seismic results provide a unique insight in the crustal Poisson's ratio structure beneath a hotspot track.

2. Seismic Data and Modeling

2.1. Wide-Angle Seismic Data

During the R/V Sonne cruise SO146-GEOPECO (*GEOPhysical Experiments at the Peruvian COntinental margin* project) in 2000, wide-angle seismic refraction and reflection data were acquired using GEOMAR ocean bottom hydrophones (OBH) and three-component ocean bottom seismometers (OBS; Bialas & Kukowski, 2000; Hampel et al., 2004). A 177-km-long profile SO146-01 was shot perpendicular to the axis of the NR at ~15°S (Figure 1). An array of two 32 l bolt air guns generated the seismic signal every 60 s, resulting in a shot-spacing of 120 m.

The data set present intra-crustal P-wave refractions (P_g) and P-wave wide-angle Moho reflections (P_mP) - which allow constraining the Moho boundary. In addition, converted intra-crustal S-wave refractions (PS_gP) and converted S-wave Moho reflections (PS_mSP) were recorded as converted waves at the sediment/basement interface on the hydrophone components (see Supporting Information Text S1 in Supporting Information S1). This wave mode is traveling through the water and sedimentary layer as a P-wave and gets converted to an S-wave at the interface between pelagic sediment and oceanic basement where the velocity contrast is higher (Figure 2; Lata & Dunn, 2020; White & Stephen, 1980; Trummer, 2002). Most of the instruments recorded good-quality data, except for station OBS 05. Otherwise, all stations show a clear signal at large offset (>100 km). See further details in the Supporting Information for seismic records (Text S1 in Supporting Information S1), shear wave conversion analysis (Text S1 in Supporting Information S1), tomographic inversion (Texts S2 and S3 in Supporting Information S1), uncertainty estimates (Text S4 in Supporting Information S1), resolution, and ambiguity tests (Text S5 in Supporting Information S1).

2.2. P- and S-Wave Tomographic Models

We used the inversion method of Korenaga et al. (2000) and Korenaga and Sager (2012) which allows the joint inversion of seismic refraction and reflection travel time data for a 2-D velocity field. The reference/initial model for the V_p inversion is based on the results of Hampel et al. (2004). Subsequently, the geometry of the Moho reflector obtained by the V_p inversion is used and held fixed in the V_s inversion. The geometry of the sedimentary unit for the V_s inversion is based on seismic reflection results (Hampel et al., 2004) consisting in a of 200–400 m thick pelagic sedimentary layer (V_p = 1.7–1.8 km/s) on top of the igneous basement. During the V_s inversion, we use damping constraints to keep fixed the V_p velocities in the sedimentary layer to invert the converted PSP crustal phases. The final inverted velocity-depth models for V_p and V_s are shown in Figures 3a and 3b, respectively.

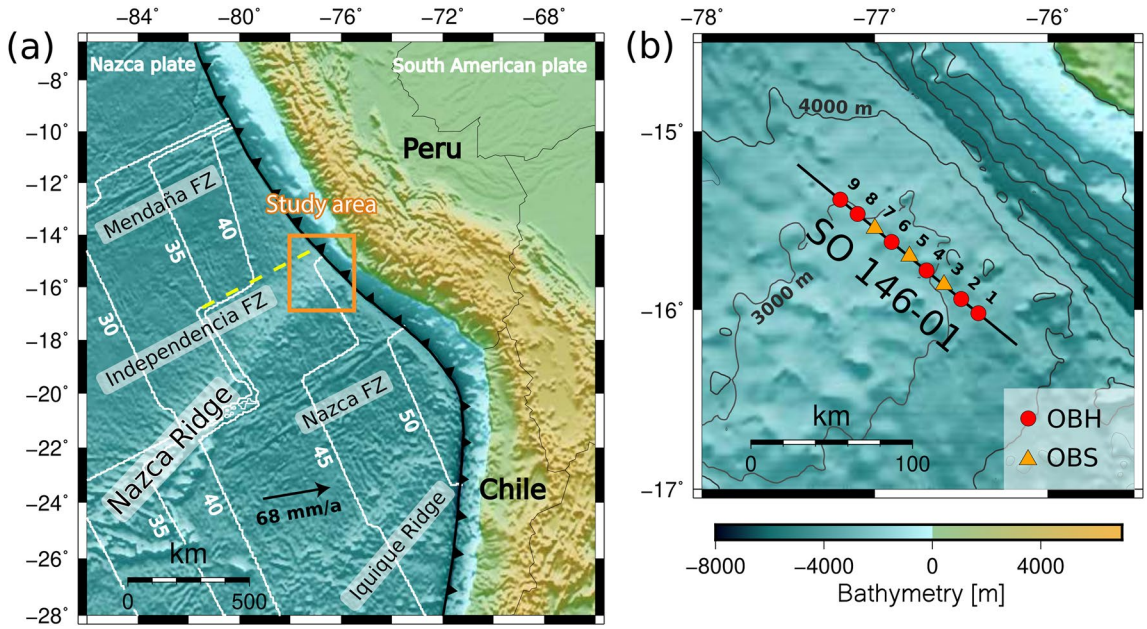

Figure 1. (a) Bathymetric map of the Nazca plate off northern Chile and southern Peru. The orange rectangle denotes the study area shown in (b). White solid lines are isochrons at 5 Ma interval (Mueller et al., 2008). Convergence rate and azimuth after Norabuena et al. (1998). The dashed yellow line shows where the Independencia Fracture Zone (FZ) is estimated according to magnetic anomaly data (Contreras-Reyes et al., 2021). (b) The solid black line denotes the studied seismic profile SO 146-01. Faint black lines show isobaths at 1000 m interval. Seismic record examples for OBS 03 are shown in Figure 2.

2.3. Poisson's Ratio Model

The Poisson's ratio ν provides valuable information for the lithological composition, porosity, fracturing, and hydration degree (Christensen, 1996), and represents the ratio of transverse contraction strain to longitudinal extension strain in the direction of stretching force. ν can be computed in terms of V_p and V_s as follows:

$$\nu = \frac{\left(\frac{V_p}{V_s}\right)^2 - 2}{2\left[\left(\frac{V_p}{V_s}\right)^2 - 1\right]}$$

The derived 2-D Poisson's ratio model is shown in Figure 3c.

3. Description of Results

Prior to describing our results, it is necessary contextualize the seismic structure of the typical oceanic crust not affected by hotspot magmatism and formed at intermediate to fast spreading rates such as the Pacific and Nazca crust. In these terms, typical oceanic crust is thought to have a similar structure as ophiolites, with extrusive basalts that overlie sheeted dikes which cap basal gabbros (e.g., Salisbury & Christensen, 1978). This litho-stratigraphic model is consistent with submersible studies of tectonic exposures and drilling samples of oceanic crust (e.g., Karson et al., 2015; Wilson et al., 2006). However, these observations are sparse, and consequently the oceanic crust structure is better known by its seismic structure, which we usually interpret in terms of the ophiolite model (e.g., Carlson, 2018; Christeson et al., 2019). Thereby, the classic seismic model for typical/normal oceanic crust in terms of the V_p structure consists in an upper crust of seismic layer 2 usually 1–1.5 km thick with a vertical V_p-gradient $\frac{dV_p}{dz}$ of 1–2 s^{-1}, and a lower crust of seismic layer 3 (4–5 km thick) with a $\frac{dV_p}{dz}$ value of 0.1 s^{-1} (Figure 4; Grevemeyer et al., 2018; Christeson et al., 2019). The uppermost crustal V_p values are highly variable in the range of 2.0–4.5 km/s at the top to values of 6.0–6.6 km/s at the layer 2/3 boundary, whereas the most common values found for the lowermost crust are 6.9–7.2 km/s (Figure 4; White et al., 1992; Grevemeyer et al., 2018; Christeson et al., 2019). For the case of oceanic crust formed at fast spreading rates, the transition

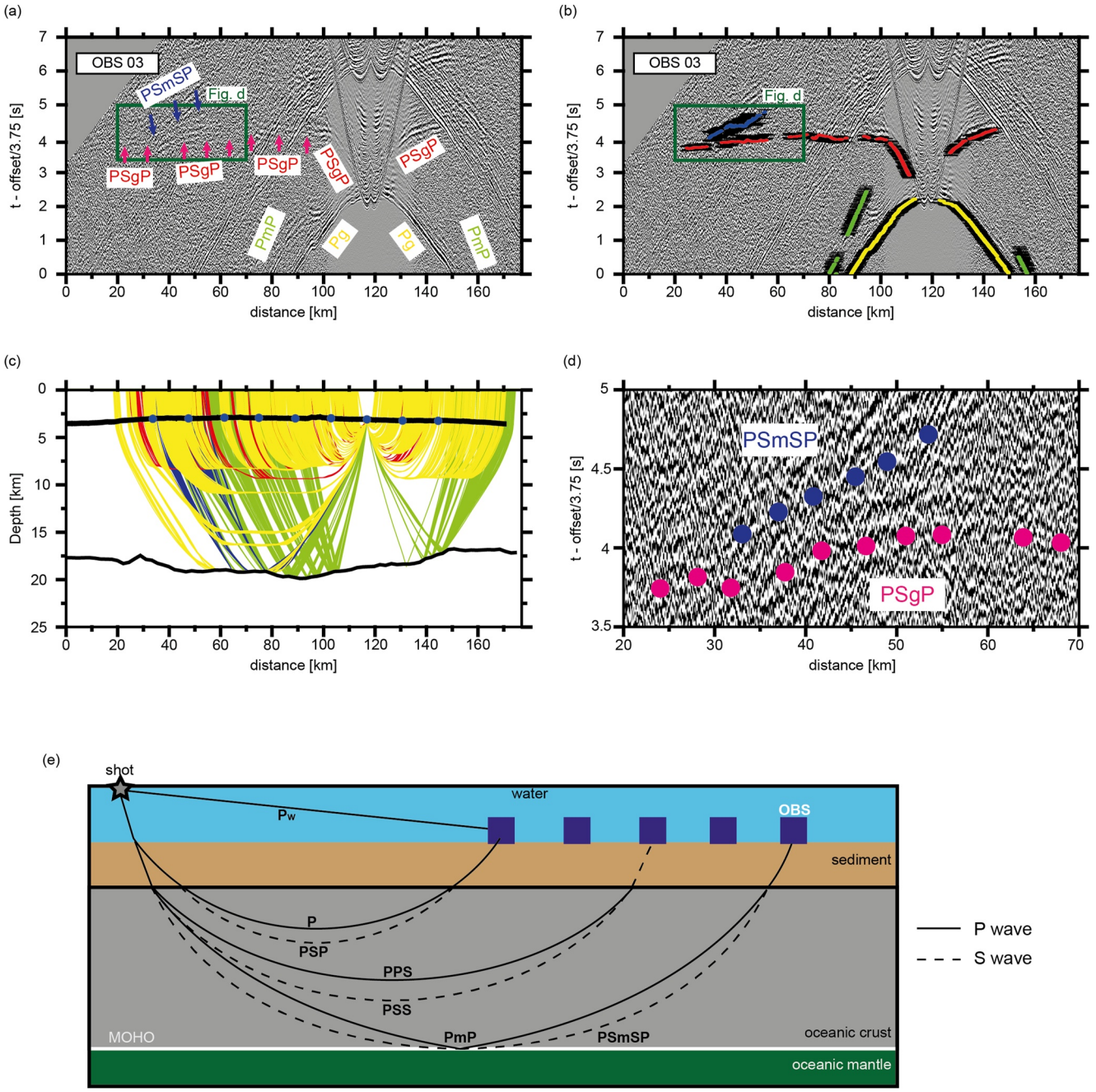

Figure 2. Example of wide-angle seismic data (OBS 03). (a) The intra-crustal P-wave refractions (P_g), P-wave wide-angle Moho reflections (P_mP), converted intra-crustal PSP-wave refractions (PS_gP) and PSP-wave Moho reflections (PS_mSP) phases were identified. See Supporting Information for details (Texts S1 and S2 in Supporting Information S1). (b) Picked (black bar error) and predicted (colored circles) travel-times. Calculated travel-times are based on the V_p and V_s models shown in Figures 3a–b. (c) Ray paths diagrams highlighting the seismic phases identified in (a). (d) Zoomed in PS_mSP phases recorded in OBS 03. (e) Schematic cartoon (not a scale) showing the nomenclature for converted waves discussed in the text.

between seismic layer 2/3 is coincident with the boundary between sheeted dikes and gabbros (Carlson, 2018). In addition, seismic studies report that the seismic layer 2 is composed mainly by two sublayers with different $\frac{dV_p}{dz}$ values of 1.0–4.0 s^{-1} and 1.0–2.0 s^{-1} for the upper layer 2A and lower layer 2B, respectively (Carlson, 2018; Christeson et al., 2019). The seismic layers 2A (<0.7 km thick) is also called the extrusive layer and is associated to basaltic lavas, whereas the layer 2B (0.5–1.5 km thick) corresponds to the sheeted dike complex (Christeson et al., 2019; Grevemeyer et al., 2018; White et al., 1992).

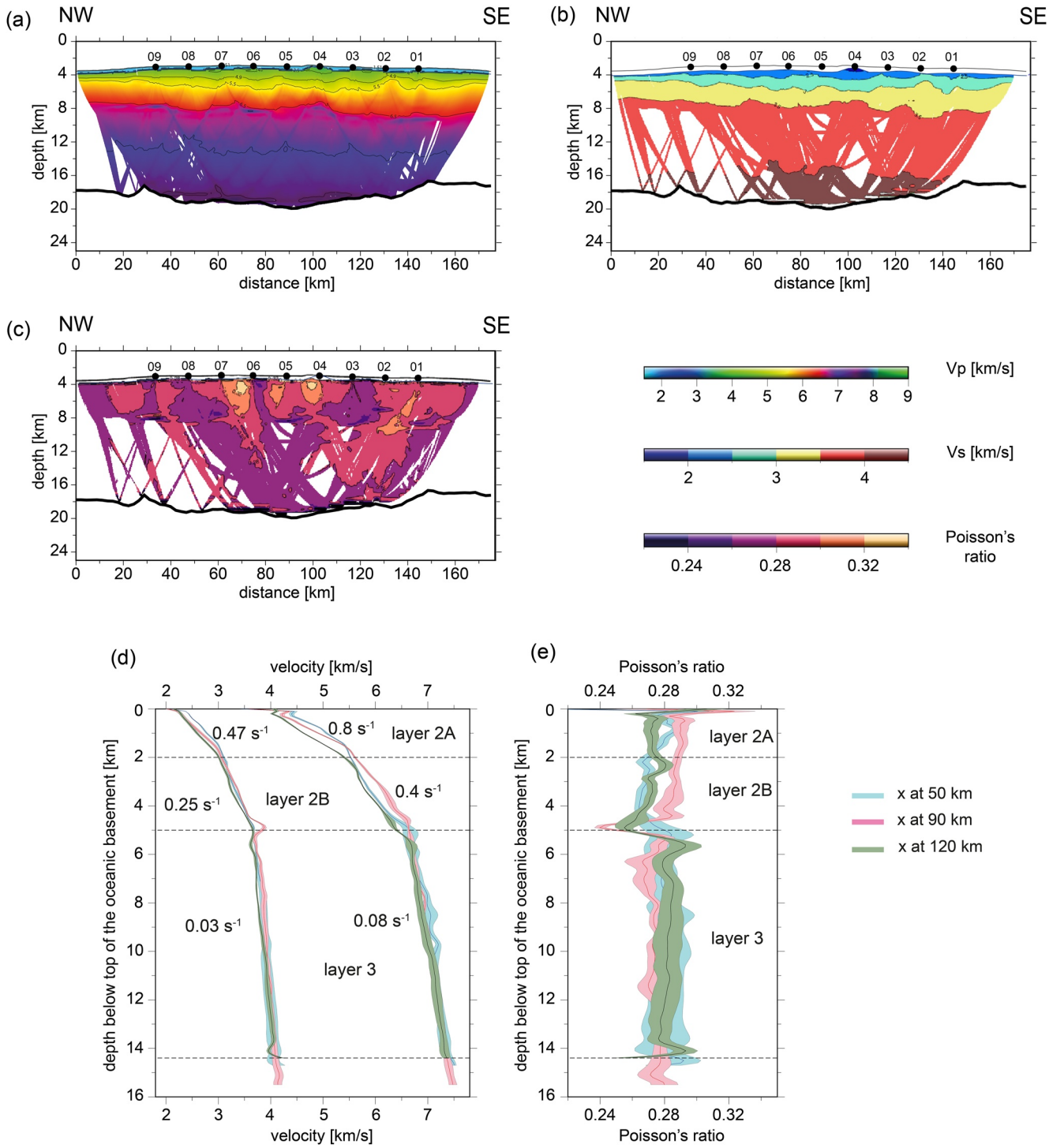

Figure 3. (a) Final 2-D V_p model, and (b), 2-D V_s model along seismic line SO146-01. (c) Derived 2-D Poisson's ratio model. See Supporting Information for the uncertainty of the models and details of the tomographic inversion (Text S4 in Supporting Information S1). (d) V_p-and V_s-depth profiles obtained along extracted vertical profiles at $x = 50$ km, 90 km, and 120 km along seismic line in (a) and (b), respectively (dotted vertical lines). The colored surrounding areas show the velocity standard deviation. The average velocity-depth gradients in s^{-1} are also shown for each layer. (e) The colored envelopes correspond to the Poisson's ratio values and their uncertainties, which are based on the V_p- and V_s-depth models shown in (d).

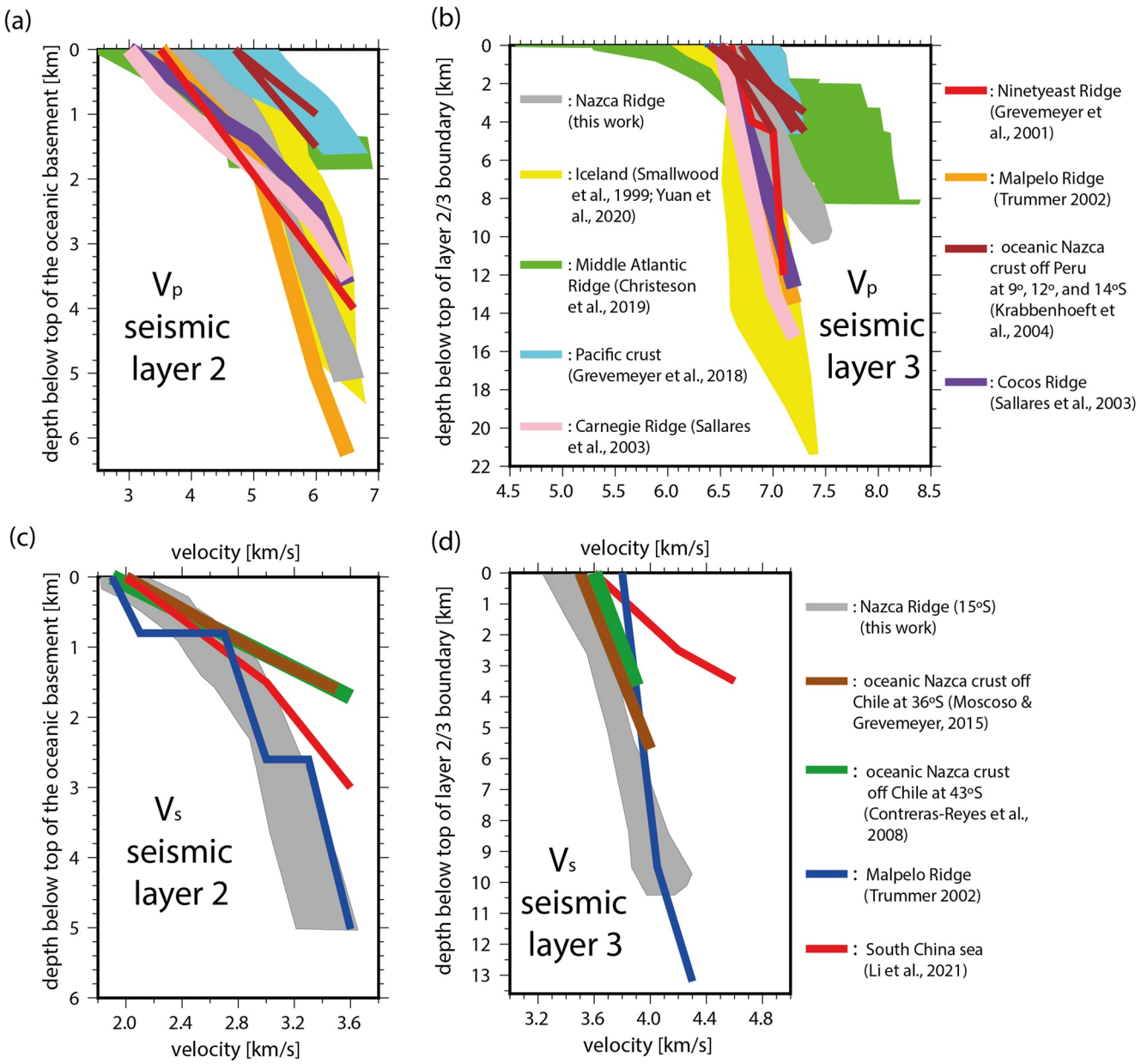

Figure 4. V_p ensembles for the (a) upper crust/seismic layer 2, and (b) lower crust/seismic layer 3. The Nazca Ridge ensemble (gray area) corresponds to the superposition of velocity-depth models at 50, 90, 120 km as is shown in Figure 3a. V_s ensembles for the (c) seismic layer 2, and (d) seismic layer 3 are also shown. The Nazca Ridge ensemble (gray area) is taken as the superposition of velocity-depth profiles at 50, 90, 120 km as is shown in Figure 3b. For comparison, we also show the velocity-depth functions of Iceland (Smallwood et al., 1999; Yuan et al., 2020), Middle Atlantic Ridge (Christeson et al., 2019), Pacific crust (Grevemeyer et al., 2018), Carnegie Ridge (Sallarès et al., 2003), Ninetyeast Ridge (Grevemeyer et al., 2001), Malpelo Ridge (Trummer, 2002), Nazca crust off Peru (Krabbenhoeft et al., 2004), South China Sea (Li et al., 2021), Cocos Ridge (Sallarès et al., 2003), and Nazca crust off Chile (Contreras-Reyes et al., 2008; Moscoso & Grevemeyer, 2015).

The V_p structure beneath the NR is composed by an anomalous ~5 km thick upper crust or seismic layer 2 with two main V_p gradients of 0.8 s^{-1} (~2 km thick) and 0.4 s^{-1} (~3 km thick), which are interpreted as the sub-layers 2A (basaltic lavas) and 2B (sheeted dikes), respectively (Figure 3). The V_p values at the top of layer 2 are 3.8–4.0 km/s and $V_p = 6.6 \pm 0.1$ km/s at the bottom with a weighted average V_p gradient of 0.56 s^{-1} in the whole seismic layer 2. The V_s model presents velocity-gradient of 0.5 and 0.3 s^{-1} for the sub-layers 2A and 2B, respectively, where the V_s values at the top and bottom of the layer 2 are 2.0–2.4 km/s and 3.6 ± 0.1 km/s, respectively (Figure 3). The Poisson's ratios at the top and bottom of seismic layer 2 vary in range values of 0.26–0.32 and 0.24–0.3, respectively (Figure 3).

The seismic layer 3 underneath the NR is characterized by V_p and V_s values in the range of 6.6–7.5 km/s and 3.6–4.0 km/s, respectively, with vertical gradient of $\frac{dV_p}{dz} = 0.08\ s^{-1}$ and $\frac{dV_s}{dz} = 0.03\ s^{-1}$. These V_p and V_s estimates result in Poisson's ratios of 0.28 ± 0.02 at the base of the crust (Figure 3). In addition, our results show that the total thickness of the oceanic crust underneath the NR is 15 ± 1 km thick, which is about 2.5 times thicker than the oceanic Nazca crust (~6 km thick) according to the results of wide-angle seismic profiles located 200–300 km north of the NR (Krabbenhoeft et al., 2004). The overthickening occurs both at the extrusive layer 2A (factor of about 3 times) and intrusive layer 2B and 3 with a factor of 2–2.5 times (Figure 3). Anomalous thick seismic layers 2 and 3 have also been observed in other hotspot tracks such as the Cocos, Malpelo. Carnegie, and Nineteyeast Ridges (Figure 4; Sallarès et al., 2003, 2005; Grevemeyer et al., 2001). In all these cases, the $\frac{dV_p}{dz}$ is clearly reduced by a 50%–70% relative to typical Pacific and Nazca oceanic crust (Figure 4).

4. Discussion

4.1. Seismic Layer 2A Beneath the Nazca Ridge

The 4.0 km/s ≤ V_p < 5.5 km/s and 2.1 km/s ≤ V_s < 3.0 km/s values (Figures 3 and 4) are consistent with the seismic layer 2A of typical oceanic Pacific and Nazca crust composed by extrusive basalts (Figure 4; Au & Clowes, 1984; Grevemeyer et al., 2018; Salisbury & Christensen, 1978). However, the layer 2A beneath the NR is ~3 times thicker implying that its V_p vertical gradient of 0.8 s^{-1} is up to 2.5 times lower than the typical $\frac{dV_p}{dz}$ for seismic layer 2A reported for typical oceanic crust not affected by hotspot magmatism (Figure 4; Christeson et al., 2019; Grevemeyer et al., 2018).

The estimated mean ν values (below the top of the oceanic basement) for the seismic layer 2A are 0.29 ± 0.02 (Figures 3 and 4), which are consistent with laboratory measurements for metabasalts in the prehnite-pumpellyite facies (ν = 0.29; Christensen, 1996), and somewhat lower than the ν values sampled for the seismic layer 2A of the Nazca crust at the southern-central Chilean outer rise at 36°S and 43°S (ν = 0.33–0.35; Contreras-Reyes et al., 2008; Moscoso & Grevemeyer, 2015). The high ν values reported by the latter authors were interpreted in terms of high degree of porosity and hydration as well as a large population of cracks caused by bending-related faulting. Because of the high heterogeneity of our estimated ν values in the uppermost crust (0.26–0.32), we cannot rule out hydrothermal alteration and/or fracturing processes in the uppermost part of layer 2A. Poisson's ratios becomes more homogeneously distributed with increasing depth within seismic layer 2A (0.28 ± 0.02) in agreement with the precipitation of secondary mineral causing the sealing of cracks in the upper crust (Grevemeyer et al., 2018). Consistently, laboratory studies show that the sealing of cracks by infill material results in an increase of both V_p and V_s (e.g., Wilkens et al., 1991), and a decrease in ν (Shaw, 1994).

4.2. Seismic Layer 2B Beneath the Nazca Ridge

The 5.5 km/s ≤ V_p < 6.6 km/s and 3.0 km/s ≤ V_s < 3.7 km/s values (Figure 3) are consistent with sheeted dikes associated to the seismic layer 2B commonly observed in the oceanic Pacific and Nazca crust (Au & Clowes, 1984; Grevemeyer et al., 2018; Salisbury & Christensen, 1978). However, the overthickening (2–2.5 times) in the seismic layer 2B beneath the NR results in a reduction of its V_p vertical gradient to 0.4 s^{-1}, which is about 2–5 times lower than the typical $\frac{dV_p}{dz}$ for seismic layer 2B of oceanic Pacific/Nazca not affected by the hotspot magmatism nor the presence of an oceanic fracture zone (Figure 4; Grevemeyer et al., 2018; Christeson et al., 2019).

At the bottom of the seismic layer 2, ν values vary largely in a range of 0.24–0.3 around the layer 2/3 boundary (Figure 3). This seismic boundary corresponds likely to the lithological contact between sheeted dikes (which deliver melt from a magma chamber) and gabbros (which form within a magma chamber) for the case of oceanic crust formed in fast-spreading centers as was concluded in the review of Christeson et al. (2019). This is the case of the oceanic crust beneath the NR where the Nazca Plate was formed at the East Pacific Rise at fast half spreading rate of 80–100 mm/yr (Mueller et al., 2008). Thus, the relatively abrupt increase in ν from 0.26 to ~0.3 at the layer 2/3 boundary (Figure 3e) likely reflects the change in mineralogy between the sheeted dikes and gabbro.

Because plagioclase crystals are lighter than the magma, it is expected that these crystals concentrate at the top of the magma chamber or axial melt lens. This location is coincident with the base of the dike sequence at seismic

layer 2/3 boundary (Vera et al., 1990). In general, the ν values for many crustal rocks increase with the content of plagioclase feldspar, where Anorthite ($\nu \sim 0.32$) and Albite ($\nu \sim 0.28$) are the end members of this mineral series (Figure 5; Abers & Hacker, 2016; Christensen, 1996). We therefore interpret the abrupt increase of ν from 0.24 to 0.3 at the seismic layer 2/3 boundary as a higher anorthite content at the top of seismic layer 3 (Figure 3).

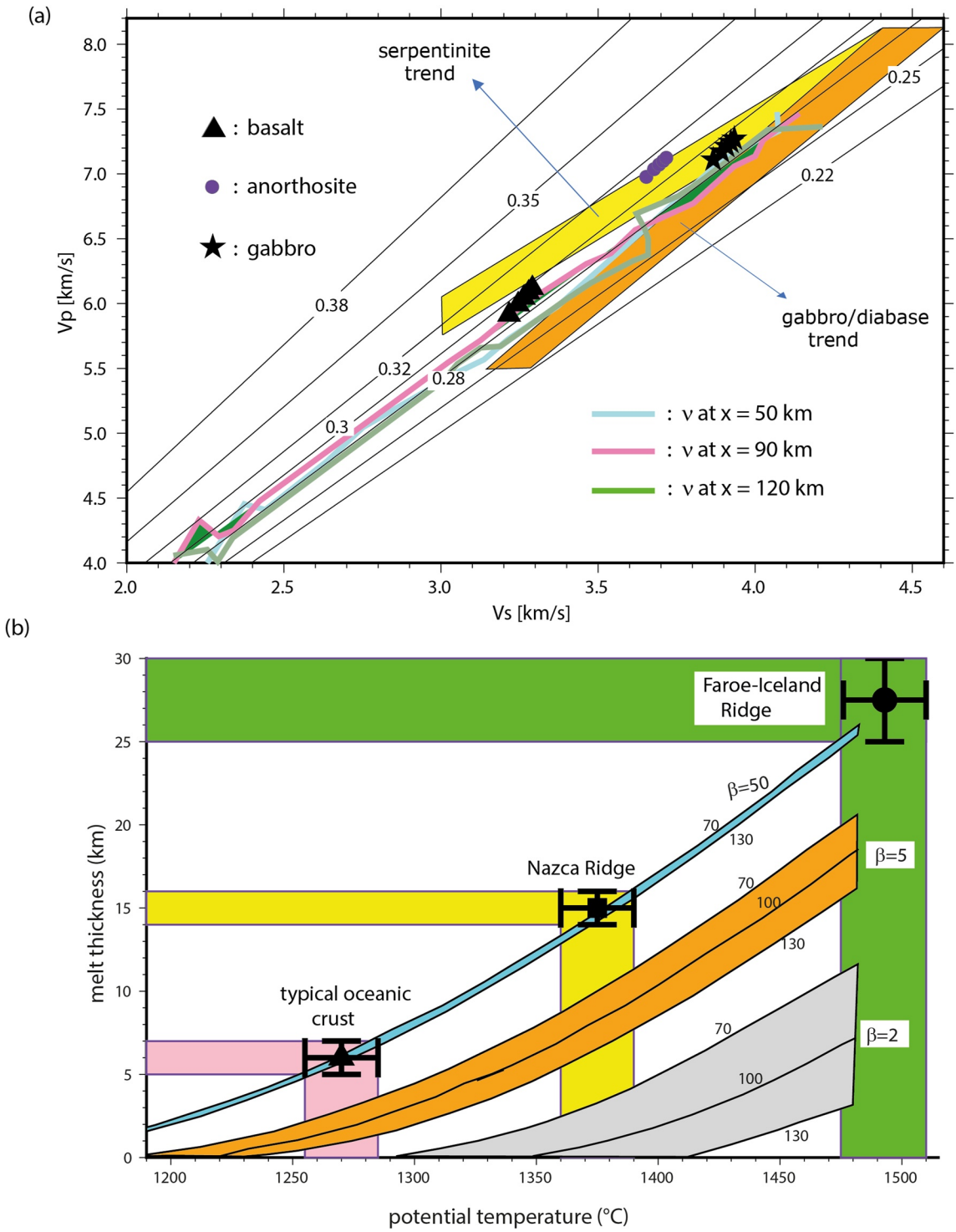

Figure 5.

4.3. Seismic Layer 3 Beneath the Nazca Ridge

The relatively low values of $\frac{dV_p}{dz} \sim 0.08\ s^{-1}$ and $\frac{dV_s}{dz} \sim 0.03\ s^{-1}$, and ν values of 0.28 ± 0.02 across the lower crust are consistent with the low porosity of gabbro with intermediate mafic/ultra-mafic composition. Christensen (1996) reported a Poisson's ratio of ~0.3 for gabbro at 200–1000 MPa (Figure 5), and he pointed out that ν is primarily controlled by mineralogy, whereas the effects caused by pressure- and temperature gradients are less than 5% and 1.1%, respectively. We explain the reduction in ν from the top (~0.3) to bottom (0.28 ± 0.02) of the gabbroic layer as the reduction in anorthite content accompanied by an increase in Mg content in pyroxenes and olivine due to Fe-Mg substitution (Christensen, 1996). In general, gabbros are rich in pyroxenes and olivine content, whereas an enrichment in the Mg-rich end members of the orthopyroxenes and olivine families after crystallization would result in decreased ν values (0.26–0.27; Abers & Hacker, 2016). The magma that crystallizes at shallow depths is primarily the residual melt produced by the magma fractionation due to separation of olivine crystals. Thus, the higher magnesium content should be higher in the lower crust at greater depth.

Furthermore, White & McKenzie (1989) showed that high potential temperature T_p anomalies in the asthenospheric mantle would produce an enrichment in the MgO and an overthickening of the oceanic crust. For instance, an increase of 200°C in T_p will result in a 10%–18% increase in Mg content and a crustal overthickening from 6 to ~25 km thick assuming a mechanical boundary layer thickness of 70–130 km and a stretching factor β of 50 (Figure 5b; White & McKenzie, 1989). T_P is defined as the temperature an adiabatically rising melt would have at the Earth's surface, whereas β is related to stretching and thinning of the lithosphere during igneous activity. A factor β of 50 is representative of the upwelling which occurs beneath oceanic spreading centers (White & McKenzie, 1989).

According to White & McKenzie, (1989), normal T_p values are 1280 ± 30°C and produce melt with the composition of mid-ocean ridge basalts. Smallwood et al. (1999) reported an anomalous crustal thickness of 25–30 km beneath the Faroe-Iceland Ridge interpreted in terms of an elevation of T_p in 200–250°C above normal if formed by passive adiabatic decompression melting (T_p of 1480–1510°C; Figure 5b). For the NR case, Contreras-Reyes et al. (2019, 2021); Hampel et al. (2004); Figure 3b), show an anomalous crustal thickness of about 15 km thick, which results in a T_p value of about 1360°–1390°C. This corresponds to an increment of approximately 100°C in T_p compared to normal oceanic Nazca crust (~6 km thick; Krabbenhoeft et al., 2004) not affected by the influence of Eastern/Salas y Gomez hotspot system (Figure 5b).

Furthermore, Smallwood et al. (1999) reported V_p/V_s ratios of 1.77 ± 0.02 (equivalent to ν values of 0.26–0.27) in the crust beneath the Faroe-Iceland Ridge. Christensen (1996) shows that ν decreases with increasing Mg content toward the Forsterite endmember closer to 0.25–0.27 as the composition becomes more ultramafic. Similarly, olivine and pyroxene rich gabbro have ν values closer to 0.27 (Abers & Hacker, 2016). Our estimates beneath the NR ($\nu \sim 0.28$) are therefore intermediate between Mg rich gabbro ($\nu = 0.27$; Faroe-Iceland Ridge case) and typical gabbroic rocks ($\nu = 0.29$–0.3; Figure 5a; Abers & Hacker, 2016; Carlson & Miller, 1997; Christensen, 1996). Despite the ν uncertainties, V_p increase clearly faster than V_s to the base of the NR crust reaching high V_p values of 7.5 ± 0.1 km/s (Figure 3; Contreras-Reyes et al., 2019; Hampel et al., 2004). These V_p values are noticeably high compared to normal gabbroic rocks ($V_p = 6.9$–7.2 km/s) and likely involves a higher component of Mg pyroxenes and forsterite (Abers & Hacker, 2016) in the lower crust beneath the NR.

Figure 5. (a) The black straight lines correspond to iso-Poisson's ratio values along V_p-V_s paths. V_p and V_s values for anorthosite, gabbro, and basalt were taken from rocks sample measurements reported by Christensen (1996) at 200, 400, 600, 800, and 1000 MPa. The gabbro/diabase and serpentinite trends were taken from the best fit of in situ seismic velocities and laboratory measurements published by Carlson and Miller (1997). The cyan/gray, pink, and light green curves were extracted from Figure 3 at 50. 90, and 120 km long profile, respectively. (b) Melt thickness generated by adiabatic decompression of the asthenospheric mantle as a function of the mantle potential temperature based on White & McKenzie (1989). The curves are shown for initial mechanical boundary layer of 70, 100, and 130 km, with crustal stretching factors β of 2 (gray area), 5 (orange area), and 50 (blue light area). A β value of 50 is representative of the upwelling of the mantle asthenosphere occurring under spreading centers (White & McKenzie, 1989). The anomalous crustal thickness of the NR (15 ± 1 km) is intermediate between normal and super thick crust formed beneath the Faroe-Iceland Ridge (Smallwood et al., 1999). The pink, yellow, and green areas represent the crustal thickness/potential temperature ranges for the formation of Pacific crust (Christeson et al., 2019; Grevemeyer et al., 2018), Nazca Ridge (Hampel et al., 2004; Contreras-Reyes et al., 2019, 2021), and Faroe Iceland Ridge (Smallwood et al., 1999; Yuan et al., 2020), respectively.

5. Conclusions

We model P-wave and converted S-wave travel-time arrivals to derive 2-D V_p and V_s tomographic models beneath the Nazca Ridge. Our seismic results lead to the following conclusions:

1. The seismic layer 2A is ~2 km thick with mean V_p- and V_s-depth gradients of $\frac{dV_p}{dz} = 0.8\ s^{-1}$ and $\frac{dV_s}{dz} = 0.5\ s^{-1}$. This layer is characterized by Poisson's ratios in the range of 0.25–0.32 at the top and 0.27–0.29 at the bottom, which are consistent with pillow lavas (extrusive basalts) characterized by a strong decrease in hydrothermal alteration and fracturing degree with depth
2. The seismic layer 2B is ~3.0 km thick with velocity gradients of $\frac{dV_p}{dz} = 0.4\ s^{-1}$ and $\frac{dV_s}{dz} = 0.25\ s^{-1}$ ν values vary from $\nu = 0.27$–0.29 (at the layer 2A/2B boundary) to $\nu = 0.24$–0.3 (layer 2B/3 boundary). The ν values for the seismic layer 2B are consistent with dolerite sheeted dykes overlying gabbroic rocks (layer 3) presenting likely a local enrichment in anorthite content at the layer 2/3 boundary
3. The seismic layer 3 is 9–11 km with relatively low velocity gradients of $\frac{dV_p}{dz} = 0.08\ s^{-1}$ and $\frac{dV_s}{dz} = 0.03\ s^{-1}$ ν values at the base of the crust are 0.28 ± 0.02, which are consistent with gabbroic rocks with an increment of Mg content (≥10% wt) compared to normal gabbroic rocks
4. The oceanic crust beneath the NR is approximately 2.5 times thicker than the typical Pacific/Nazca crust, whereas overthickening occurs both at the extrusive and intrusive layers. The anomalously thick crust of the NR (~15 km thick) is consistent with an increase in the asthenospheric mantle potential temperature of about 100°C formed by passive adiabatic decompression in the asthenospheric mantle

Data Availability Statement

The readers can access to our seismic results at the following link: https://doi.org/10.17605/OSF.IO/B6X8E.

Acknowledgments
We acknowledge the support of the Chilean National Science Foundation (FONDECYT) grants 1170009 and 1210101. We thank six anonymous reviewers, a seventh reviewer (Brandon Shuck), and the associated Editor Harm van Avendonk and Lucy Flesh for their in-depth reviews. We also thank fruitful discussions with Juan-Pablo González-Bello.

References

Abers, G. A., & Hacker, B. R. (2016). A MATLAB toolbox and Excel workbook for calculating the densities, seismic wave speeds, and major element composition of minerals and rocks at pressure and temperature. *Geochemistry, Geophysics, Geosystems*, *17*(2), 616–624. https://doi.org/10.1002/2015GC006171

Au, D., & Clowes, R. M. (1984). Shear-wave velocity structure of the oceanic lithosphere from ocean bottom seismometer studies. *Geophysical Journal International*, *77*(1), 105–123. https://doi.org/10.1111/j.1365-246X.1984.tb01927.x

Bello-González, J. P., Contreras-Reyes, E., & Arriagada, C. (2018). Predicted path for hotspot tracks off South America since Paleocene times: Tectonic implications of ridge-trench collision along the Andean margin. *Gondwana Research*, *64*, 216–234. https://doi.org/10.1016/j.gr.2018.07.008

Bialas, J., & Kukowski, N. (Eds.), (2000). *Cruise report SO146/1&2 geopeco: GEOphysical experiments at the PEruvian COntinental margin investigations of tectonics, mechanics, gashydrates, and fluid transport; Arica- Talcahuano, March 1 - May 4, 2000. Open access. GEOMAR-report*. GEOMAR Forschungszentrum für marine Geowissenschaften. https://doi.org/10.3289/GEOMAR_REP_096_2000

Caress, D. W., McNutt, M. K., Detrick, R. S., & Mutter, J. C. (1995). Seismic imaging of hotspot-related crustal underplating beneath the Marquesas Islands. *Nature*, *373*(6515), 600–603. https://doi.org/10.1038/373600a0

Carlson, R. L. (2018). Ocean crustal seismic layer 2C. *Geochemistry, Geophysics, Geosystems*, *19*(9), 3084–3096. https://doi.org/10.1029/2018GC007614

Carlson, R. L., & Miller, D. J. (1997). A new assessment of the abundance of serpentinite in the oceanic crust. *Geophysical Research Letters*, *24*(4), 457–460. https://doi.org/10.1029/97gl00144

Charvis, P., Laesanpura, A., Gallart, J., Hirn, A., Lépine, J. C., De Voogd, B., et al. (1999). Spatial distribution of hotspot material added to the lithosphere under La Réunion, from wide-angle seismic data. *Journal of Geophysical Research*, *104*(B2), 2875–2893. https://doi.org/10.1029/98jb02841

Christensen, N. I. (1996). Poisson's ratio and crustal seismology. *Journal of Geophysical Research*, *101*(B2), 3139–3156. https://doi.org/10.1029/95JB03446

Christeson, G. L., Goff, J. A., & Reece, R. S. (2019). Synthesis of oceanic crustal structure from two-dimensional seismic profiles. *Reviews of Geophysics*, *57*(2), 504–529. https://doi.org/10.1029/2019rg000641

Contreras-Reyes, E., Cortés-Rivas, V., Manríquez, P., & Maksymowicz, A. (2021). The silent bending of the oceanic Nazca Plate at the Peruvian Trench. *Tectonophysics*, *807*, 228810. https://doi.org/10.1016/j.tecto.2021.228810

Contreras-Reyes, E., Grevemeyer, I., Flueh, E. R., Scherwath, M., & Bialas, J. (2008). Effect of trench-outer rise bending-related faulting on seismic Poisson's ratio and mantle anisotropy: A case study offshore of southern Central Chile. *Geophysical Journal International*, *173*(1), 142–156. https://doi.org/10.1111/j.1365-246X.2008.03716.x

Contreras-Reyes, E., Grevemeyer, I., Watts, A. B., Planert, L., Flueh, E. R., & Peirce, C. (2010). Crustal intrusion beneath the Louisville hotspot track. *Earth and Planetary Science Letters*, *289*(3–4), 323–333. https://doi.org/10.1016/j.epsl.2009.11.020

Contreras-Reyes, E., Muñoz-Linford, P., Cortés-Rivas, V., Bello-González, J. P., Ruiz, J. A., & Krabbenhoeft, A. (2019). Structure of the collision zone between the Nazca ridge and the Peruvian convergent margin: Geodynamic and seismotectonic implications. *Tectonics*, *38*(9), 3416–3435. https://doi.org/10.1029/2019TC005637

Fujie, G., Kodaira, S., Yamashita, M., Sato, T., Takahashi, T., & Takahashi, N. (2013). Systematic changes in the incoming plate structure at the Kuril trench. *Geophysical Research Letters*, *40*(1), 88–93. https://doi.org/10.1029/2012GL054340

Grevemeyer, I., Flueh, E. R., Reichert, C., Bialas, J., Kläschen, D., & Kopp, C. (2001). Crustal architecture and deep structure of the Nineyeast Ridge hotspot trail from active-source ocean bottom seismology. *Geophysical Journal International*, *144*(2), 414–431. https://doi.org/10.1046/j.0956-540x.2000.01334.x

Grevemeyer, I., Ranero, C. R., & Ivandic, M. (2018). Structure of oceanic crust and serpentinization at subduction trenches. *Geosphere*, *14*(2), 395–418. https://doi.org/10.1130/ges01537.1

Hampel, A., Kukowski, N., Bialas, J., Huebscher, C., & Heinbockel, R. (2004). Ridge subduction at an erosive margin: The collision zone of the Nazca Ridge in southern Peru. *Journal of Geophysical Research*, *109*(B2). https://doi.org/10.1029/2003JB002593

Hyndman, R. D. (1979). Poisson's ratio in the oceanic crust—A review. *Tectonophysics*, *59*(1–4), 321–333. https://doi.org/10.1016/0040-1951(79)90053-2

Kaneda, K., Kodaira, S., Nishizawa, A., Morishita, T., & Takahashi, N. (2010). Structural evolution of preexisting oceanic crust through intraplate igneous activities in the Marcus-Wake seamount chain. *Geochemistry, Geophysics, Geosystems*, *11*(10). https://doi.org/10.1029/2010GC003231

Karson, J. A., Kelley, D. S., Fornari, D. J., Perfit, M. R., & Shank, T. M. (2015). *Discovering the deep: A photographic Atlas of the seafloor and oceanic crust*. Cambridge University Press.

Kopp, H., Flueh, E. R., Papenberg, C., & Klaeschen, D. (2004). Seismic investigations of the O'Higgins seamount group and juan Fernández Ridge: Aseismic ridge emplacement and lithosphere hydration. *Tectonics*, *23*(2). https://doi.org/10.1029/2003TC001590

Korenaga, J., Holbrook, W. S., Kent, G. M., Kelemen, P. B., Detrick, R. S., Larsen, H.-C., et al. (2000). Crustal structure the southeast Greenland margin from joint refraction and reflection seismic tomography. *Journal of Geophysical Research*, *105*(B9), 21591–21614. https://doi.org/10.1029/2000JB900188

Korenaga, J., & Sager, W. W. (2012). Seismic tomography of Shatsky Rise by adaptive importance sampling. *Journal of Geophysical Research*, *117*(B8). https://doi.org/10.1029/2012JB009248

Krabbenhoeft, A., Bialas, J., Kopp, H., Kukowski, N., & Hübscher, C. (2004). Crustal structure of the Peruvian continental margin from wide-angle seismic studies. *Geophysical Journal International*, *159*(2), 749–764. https://doi.org/10.1111/j.1365-246x.2004.02425.x

Kumar, A., Wagner, L. S., Beck, S. L., Long, M. D., Zandt, G., Young, B., et al. (2016). Seismicity and state of stress in the central and southern Peruvian flat slab. *Earth and Planetary Science Letters*, *441*, 71–80. https://doi.org/10.1016/j.epsl.2016.02.023

Lata, C., & Dunn, R. A. (2020). Uppermost crustal structure across the eastern Lau spreading center from P-to-S converted waves. *Marine Geophysical Researches*, *41*(4), 1–20. https://doi.org/10.1007/s11001-020-09419-5

Li, Y., Grevemeyer, I., Huang, H., Qiu, X., & Xu, Z. (2021). Seismic constraint from V_p/V_s ratios on the structure and composition across the continent-ocean transition zone, South China Sea. *Geophysical Research Letters*, *48*(16), e2021GL094656. https://doi.org/10.1029/2021gl094656

Moscoso, E., & Grevemeyer, I. (2015). Bending-related faulting of the incoming oceanic plate and its effect on lithospheric hydration and seismicity: A passive and active seismological study offshore Maule, Chile. *Journal of Geodynamics*, *90*, 58–70. https://doi.org/10.1016/j.jog.2015.06.007

Mueller, R. D., Sdrolias, M., Gaina, C., & Roest, W. R. (2008). Age, spreading rates, and spreading asymmetry of the world's ocean crust. *Geochemistry, Geophysics, Geosystems*, *9*(4). https://doi.org/10.1029/2007GC001743

Naar, D. F., & Hey, R. N. (1986). Fast rift propagation along the East Pacific Rise near Easter Island. *Journal of Geophysical Research*, *91*(B3), 3425–3438. https://doi.org/10.1029/JB091iB03p03425

Norabuena, E., Leffler-Griffin, L., Mao, A., Dixon, T., Stein, S., Sacks, I. S., et al. (1998). Space geodetic observations of Nazca-South America convergence across the central Andes. *Science*, *279*(5349), 358–362. https://doi.org/10.1126/science.279.5349.358

Richards, M., Contreras-Reyes, E., Lithgow-Bertelloni, C., Ghiorso, M., & Stixrude, L. (2013). Petrological interpretation of deep crustal intrusive bodies beneath oceanic hotspot provinces. *Geochemistry, Geophysics, Geosystems*, *14*(3), 604–619. https://doi.org/10.1029/2012GC004448

Salisbury, M. H., & Christensen, N. I. (1978). The seismic velocity structure of a traverse through the Bay of Islands ophiolite complex, Newfoundland, an exposure of oceanic crust and upper mantle. *Journal of Geophysical Research*, *83*(B2), 805–817. https://doi.org/10.1029/jb083ib02p00805

Sallarès, V., Charvis, P., Flueh, E. R., & Bialas, J. (2003). Seismic structure of Cocos and Malpelo Volcanic Ridges and implications for hot spot-ridge interaction. *Journal of Geophysical Research*, *108*(B12). https://doi.org/10.1029/2003JB002431

Sallarès, V., Charvis, P., Flueh, E. R., Bialas, J., & SALIERI Scientific Party. (2005). Seismic structure of the Carnegie ridge and the nature of the Galapagos hotspot. *Geophysical Journal International*, *161*(3), 763–788. https://doi.org/10.1111/j.1365-246X.2005.02592.x

Shaw, P. R. (1994). Age variations of oceanic crust Poisson's ratio: Inversion and a porosity evolution model. *Journal of Geophysical Research*, *99*(B2), 3057–3066. https://doi.org/10.1029/93JB02109

Shuck, B. D., van Avendonk, H. J. A. V., & Bécel, A. (2019). The role of mantle melts in the transition from rifting to seafloor spreading offshore eastern North America. *Earth and Planetary Science Letters*, *525*, 115756. https://doi.org/10.1016/j.epsl.2019.115756a

Smallwood, J. R., Staples, R. K., Richardson, K. R., & White, R. S. (1999). Crust generated above the Iceland mantle plume: From continental rift to oceanic spreading center. *Journal of Geophysical Research*, *104*(B10), 22885–22902. https://doi.org/10.1029/1999jb900176

Trummer, I. (2002). *S-wave processing and interpretation of wide-angle seismic refraction data, Malpelo ridge, eastern Panama basin (Doctoral dissertation)*.

Vera, E. E., Mutter, J. C., Buhl, P., Orcutt, J. A., Harding, A. J., Kappus, M. E., et al. (1990). The structure of 0-to 0.2-my-old oceanic crust at 9°N on the East Pacific Rise from expanded spread profiles. *Journal of Geophysical Research*, *95*(B10), 15529–15556. https://doi.org/10.1029/JB095iB10p15529

Wagner, L. S., Caddick, M. J., Kumar, A., Beck, S. L., & Long, M. D. (2020). Effects of oceanic crustal thickness on intermediate depth seismicity. *Frontiers of Earth Science*, *8*, 244. https://doi.org/10.3389/feart.2020.00244

Walther, C. H. (2003). The crustal structure of the Cocos ridge off Costa Rica. *Journal of Geophysical Research*, *108*(B3). https://doi.org/10.1029/2001JB000888

Watts, A. B., Grevemeyer, I., Shillington, D. J., Dunn, R. A., Boston, B., & Gómez de La Peña, L. (2021). Seismic structure, gravity anomalies and flexure along the emperor seamount chain. *Journal of Geophysical Research: Solid Earth*, *126*(3), e2020JB021109. https://doi.org/10.1029/2020jb021109

Weigel, W., & Grevemeyer, I. (1999). The Great meteor seamount: Seismic structure of a submerged intraplate volcano. *Journal of Geodynamics*, *28*(1), 27–40. https://doi.org/10.1016/S0264-3707(98)00030-1

White, R., & McKenzie, D. (1989). Magmatism at rift zones: The generation of volcanic continental margins and flood basalts. *Journal of Geophysical Research: Solid Earth*, *94*(B6), 7685–7729. https://doi.org/10.1029/JB094iB06p07685

White, R. S., McKenzie, D., & O'Nions, R. K. (1992). Oceanic crustal thickness from seismic measurements and rare Earth element inversions. *Journal of Geophysical Research*, *97*, 19683–19715. https://doi.org/10.1029/92jb01749

White, R. S., & Stephen, R. A. (1980). Compressional to shear wave conversion in oceanic crust. *Geophysical Journal International*, *63*(2), 547–565. https://doi.org/10.1111/j.1365-246x.1980.tb02637.x

Wilkens, R. H., Fryer, G. J., & Karsten, J. (1991). Evolution of porosity and seismic structure of upper oceanic crust: Importance of aspect ratios. *Journal of Geophysical Research*, *96*(B11), 17981–17995. https://doi.org/10.1029/91JB01454

Wilson, D. S., Teagle, D. A. H., Alt, J. C., Banerjee, N. R., Umino, S., Miyashita, S., et al. (2006). Drilling to gabbro in intact ocean crust. *Science*, *312*(5776), 1016–1020. https://doi.org/10.1126/science.1126090

Yuan, X., Korenaga, J., Holbrook, W. S., & Kelemen, P. B. (2020). Crustal structure of the Greenland-Iceland Ridge from joint refraction and reflection seismic tomography. *Journal of Geophysical Research: Solid Earth*, *125*(7), e2020JB019847. https://doi.org/10.1029/2020jb019847